Pergamon

Int. J. Solids Structures Vol. 35, Nos 9–10, pp. 799–813, 1998

0020–7683/98 $19.00 + .00

PII: S0020–7683–(97)00085–1

FINITE ELEMENT ANALYSIS OF INTERFACIAL CRACK PROPAGATION BASED ON LOCAL SHEAR, PART I—NEAR TIP DEFORMATION

MARTIN Y. M. CHIANG
Polymers Division, National Institute of Standards and Technology, BLDG 224, Rm A, Gaithersburg, MD 20899, U.S.A.

and

HERZL CHAI
Department of Solid Mechanics, Materials and Structures, Tel-Aviv University, Tel-Aviv, Israel

(*Received* 3 *May* 1996; *in revised form* 14 *February* 1997)

Abstract—Full-field, plane-strain elastoplastic solutions for an interface crack in adhesive bonds deforming in shear are obtained from a finite element analysis. The analysis, which considers very large strains and includes the effect of contact and friction between the debonded interfaces, is particularized to a nearly elastic ideally-plastic interlayer obeying J_2 flow, which is sandwiched between either rigid or compliant substrates. Guided by experimental evidence, the analysis focuses on the interface ahead of the crack tip, where crack propagation occurs. The engineering shear strain at the crack tip along the interface, γ, is characterized by a power-law singularity of the form $\gamma = K(x/h)^{-\delta}$, where h is the bond thickness, x is the horizontal axis originating from the crack tip and K and δ are the numerically obtained functions of bond-average shear strain, $\bar{\gamma}$. The singular field under small-scale yielding ($\delta = 1$) is maintained up to $\bar{\gamma} = 0.03 \sim 0.05$, which is close to the yield strain in shear of the adhesive (0.06). For larger remote shear strains, the strength of the singularity monotonically decreases with $\bar{\gamma}$. This apparently new characteristic results from the interaction of the deformation field at the crack tip with the opposing interface of the bond. The distribution of shear strain ahead of the crack tip compares well with experimental results. The effect of interfacial friction appears to be significant only for relatively large loading ($\bar{\gamma} > 0.2$).

1. INTRODUCTION

This two-part report presents the analytical counterpart of a combined experimental (Chai and Chiang, 1996) and finite element effort to establish a crack propagation criterion for adhesive bonds subjected to shear which is independent of the specimen geometry and the bond thickness. The aforementioned tests show that the fracture process in shear loaded adhesive joints (i.e. the Butterfly and the end-notched flexure (ENF) adhesive bonding specimens shown in Fig. 1) is characterized by a stable crack propagation followed by catastrophic growth. During the stable growth, a variety of failure mechanisms may be activated at or ahead of the crack tip, the most predominant one being interfacial cracking. One of the more interesting aspects of the latter phenomenon is the development of very large shear strains (i.e. over unity) over a considerable region ahead of the crack tip even though the deformation in the rest of the bond may remain small (Chai, 1992; Chiang and Chai, 1994). Consequently, the singular behavior predicted by linear elastic fracture mechanics (LEFM) or by the HRR theory may be inapplicable. It is the purpose of this work to try to develop an effective analytical fracture mechanics approach for treating very large deformations which, combined with the above mentioned experimental work, can lead to a valid crack propagation criterion.

The majority of early analyses of shear failure of adhesive bonds are based either on the shear lag concept, which neglects the stress variations across the bond [e.g. Goland and Reissner (1944); Hart-Smith (1981)] or LEFM [e.g. Malyshev and Salganic (1965); Wang and Yuan (1982)]. More recently, small scale yielding solutions have been reported for

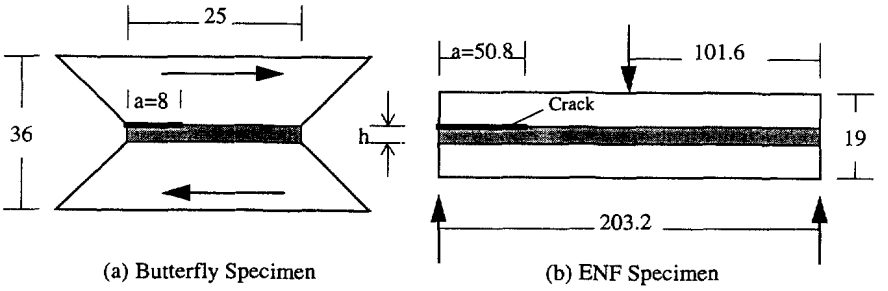

(a) Butterfly Specimen (b) ENF Specimen

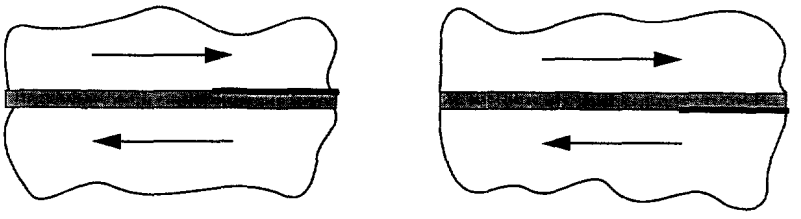

(c) CSIC Rigid-Substrates Model (d) TSIC Rigid-Substrates Model

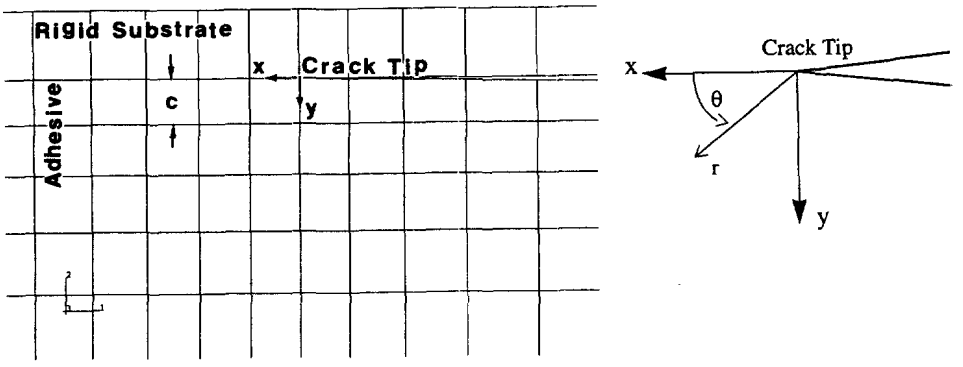

(e) Crack Tip Mesh and Coordinates

Fig. 1. The Butterfly (a) and the ENF (b) adhesive bonding test specimens used in the experiments [Chai and Chiang (1996)]. (c) and (d) rigid-substrates adhesive bond models. (e) crack tip mesh.

bimaterial interface crack problems [e.g. Shih and Asaro (1988); Zywicz and Parks (1990); Sharma and Aravas (1991)]. Such solutions, however, are still insufficient to account for the very large deformations discussed above. In a more closely related work, Varias *et al.* (1992) presented elastoplastic finite element solutions for a constrained interlayer containing a crack at the center of the bond. That work, which considered a combined tension and shear loading, was also limited to remote strains less than the yield strain of the adhesive. That work was also limited to remote shear strains less than the yield strain of the adhesive.

The present study is carried out using a large strain, incremental plasticity finite element analysis which incorporates the effect of strain rate on the adhesive yielding and the effect of interfacial friction along the debonded interface. In addition to the ENF specimen, analyses are performed on the rigid-substrates models (Fig. 1). This simplification is deemed appropriate considering the large stiffness mismatch between the interlayer and the aluminium adherends used in the fracture tests (i.e. $E_{al}/E_{ad} \approx 20$, where E_{al} and E_{ad} are the Young's moduli for the aluminium and the adhesive, respectively). The association between the rigid-substrates and the ENF or the Butterfly joints is made on the basis of equal bond-average shear strain at the crack tip region $\bar{\gamma}_t$; the latter quantity was recorded in the aforementioned tests. Two configurations of interfacial precrack, i.e. the CSIC (compressions side interface crack) and the TSIC (tension side interface crack), see Fig. 1(c),(d),

are analyzed. This part is concerned with a stationary crack. The stable crack propagation phase, which includes interfacial cracking and other failure modes, is reported in Part II.

The numerical analysis and the material models used are described in Section 2 while the deformation at the crack tip is treated in Section 3. Section 4 provides a comparison with experimental evidence while Section 5 contains a summary and conclusions. The experimental work concerning the friction law for the debonded interfaces and the adhesive rate dependence are described in the Appendices.

2. NUMERICAL ANALYSIS

The Abaqus† (HKS, 1994) finite element program is employed. Plane-strain conditions are assumed for the ENF and the rigid-substrates models. Naturally, the elastoplastic problem for the rigid-substrates models is made independent of the bond thickness, h, by normalizing the coordinate axes, x, y, emanating from the crack tip [Fig. 1(e)] by h. Thus, for a given bond-average shear strain, all field quantities at a point $(x/h, y/h)$ in the bond are independent of h. It is known that the singular stress field for linearly elastic crack problems can be accurately predicted using special finite element techniques [e.g. Wang and Yuan (1983); Kuo and Wang (1985); Stolarski and Chiang (1989)]. Such techniques may not apply, however, in the present large deformation problem. Therefore, despite its slow convergence rate, a standard finite element analysis which utilizes very fine crack tip mesh is adopted in this study.

2.1. *Mesh*

Four-node isoparametric elements are used, the dimensions of which gradually decrease toward the crack tip [Fig. 1(e)]. The thickness of the bond contains 10 elements. Consistent with experimental observations and in order to ascertain valid solutions as close to the crack tip as possible, no crack tip blunting provisions are made. The solution convergence is assessed by employing various mesh refinements. The latter are characterized by the ratio c/h, where c is the dimension of the square element right at the crack tip [Fig. 1(e)].

2.2. *Materials and material model*

The adherends are 7075-T6 aluminum alloy while the adhesive is BP 907 (American Cyanamid Co.), a toughened, mildly ductile epoxy having a Young's modulus approximately 5% that of the aluminum adherends. The Young's modulus and the Poisson's ratio for the ENF adherends are taken as 69 GPa and 0.3, respectively. In order to facilitate a direct comparison with the experiments, all material parameters for the adhesive used in the finite element program (including the adhesive stress–strain behavior, the coefficient of friction between the debonded interfaces and the adhesive rate dependence) are experimentally determined. The experimental scatter is deemed less than 10%.

The stress vs strain curve in shear for the adhesive was established using the napkin ring adhesive joint specimen (Chai, 1993). It was found that this curve is little affected by the bond thickness over the range $40\ \mu\text{m} < h < 420\ \mu\text{m}$. The representative curve, reproduced in Fig. 2, exhibits a nearly elastic perfectly-plastic behavior, with the yield strain $\gamma_Y = 0.06$. The adhesive is assumed to obey J_2 plasticity with isotropic strain hardening. Although the yielding behavior of polymeric materials is generally pressure dependent, a previous study (Chiang and Chai (1994)) showed that the effect of pressure sensitivity on global mechanical responses such as specimen deflection and plastic zone length is small. Consequently, this effect is not considered in this work.

The numerical program accepts as input the stress–strain relationship in uniaxial tension. The latter was established by running Abaqus on a simple shear configuration utilizing a trial and error input procedure until the experimental shear stress vs shear strain

† Certain commercial software, materials and equipment are identified in this paper in order to specify adequately the experimental procedure. In no case does such identification imply recommendation or endorsement by the National Institute of Standards and Technology (NIST) nor does it imply necessarily the best available for the purpose.

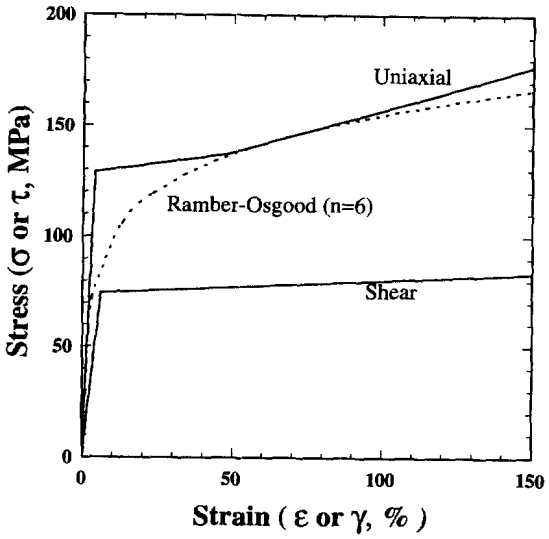

Fig. 2. The experimentally obtained stress–strain curve in shear [e.g.Chai (1993)] and the deduced uniaxial compression curve for the modeled interlayer. Also shown for comparison purposes is a Ramberg–Os good material representation with $n = 6$.

curve was recovered. The uniaxial stress–strain curve obtained in this way is shown in Fig. 2. Also shown in this figure, for comparative purposes, is an approximation of this curve based on a Ramberg–Osgood representation with a hardening exponent, $n = 6$.

2.3. *Material rate*

In this analysis, the dependence of the adhesive yield stress on the strain rate is characterized by

$$\dot{\varepsilon}^{\mathrm{pl}} = D(\sigma/\sigma_0 - 1)^{\mathrm{d}}, \tag{1}$$

where $\dot{\varepsilon}^{\mathrm{pl}}$ is the time derivative of the equivalent plastic strain, σ_0 and σ are the equivalent quasistatic and concurrent yield stresses, respectively, and D and d are material parameters. Equation (1) has been used in a number of analyses of dynamic plastic deformation [e.g. Ting and Symonds (1962)]. This rate law implies that the fractional increase in stress above the static yield stress σ_0 at a given strain is a simple function of the strain rate. As shown in Appendix A, the rate for the present adhesive is well represented by eqn (1) with $D = 10.5$ and $d = 3.7$.

2.4. *Friction law*

Tests were carried out (Appendix B) to quantify the effect of friction between the debonded interfaces. Adopting a Coulomb friction model, the friction coefficient, μ, was determined from

$$\mu = F_{\mathrm{sc}}/F_{\mathrm{n}}, \tag{2}$$

where F_{n} is the applied normal force and F_{sc} is the shearing force needed to initiate sliding. As shown in Fig. B1, a friction coefficient of 0.34 seem to characterize reasonably well the behavior for all bond thicknesses and normal stress levels employed. This value is used in the finite element program.

3. RESULTS

According to LEFM, the strain (or stress) field in a cracked body is characterized by a r^{δ} type [or more than one type, see Ting and Chou (1981); Stolarski and Chiang (1989); Ting (1996)] singularity according to:

$$\varepsilon_{ij} = Kr^{-\delta} f_{ij}(\theta) + \text{other terms} \tag{3}$$

where ε_{ij} is a strain tensor, K is a constant, r and θ are polar coordinates [Fig. 1(e)] and f_{ij} is a dimensionless function of θ. The most important characteristic of the singular term in eqn (3) is that the stress field at the crack tip is identical in form for all loadings, with the latter being reflected through K. Thus, the local stress field is characterized by K and a critical value can be used as a fracture criterion. For finite strain problems, the existence of such a form, to the authors' knowledge, is still questionable. Consequently, a thorough characterization of the deformation fields in the bond is a difficult task. However, it is found in this study that eqn (3) may still characterize well the deformation along the interface ahead of the crack tip even under general nonlinear conditions. As shown in Part II, such a characterization seem to be sufficient for establishing a viable crack propagation criterion.

3.1. *Rigid-substrates models*

In the finite element analysis, the nodal points for the lower interface are held fixed while the nodes of the upper interface are given a uniform horizontal displacement. No external constraints on the rotation of the upper substrate are imposed. The sole loading parameter in this case is the average shear strain across the bond, $\bar{\gamma}$ ("load", i.e. the relative shear displacement across the bond divided by the bond thickness).

The engineering shear strain along the interface, γ, is calculated from the slope of the initially vertical grid lines (i.e. the relative horizontal displacement shift of a line divided by the concurrent element thickness) associated with the first row of elements in the interlayer. Figure 3 shows the distribution of γ along the interface ahead of the crack tip for a given load ($\bar{\gamma} = 0.3$). The data are presented on a log–log scale in order to help identify a simple power law singularity. Results are given for five levels of mesh refinement, i.e. $c/h = 0.005$, 0.01, 0.02, 0.04 and 0.06. It is evident that the finest mesh provides a convergent solution at least as close as a tenth bond thickness from the crack tip. The finest mesh ($c/h = 0.005$) was chosen for all subsequent analyses. Figure 3 shows that as the mesh is refined, the curves maintain their straightness closer and closer to the crack tip. This indicates a $x^{-\delta}$

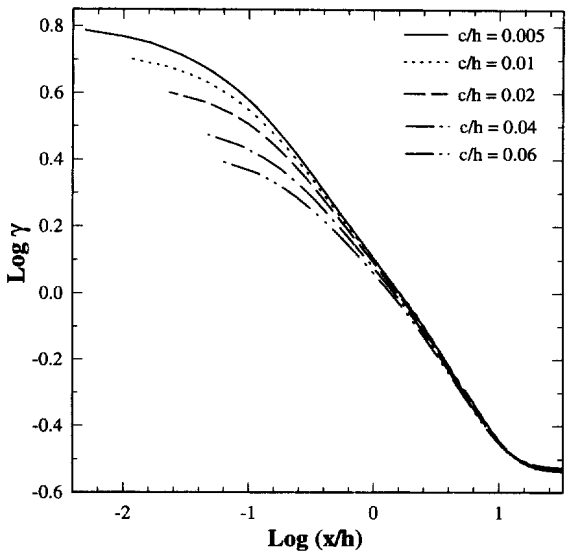

Fig. 3. The distribution of engineering shear strain along the interface ahead of the crack tip for five levels of mesh refinement—CSIC rigid-substrates model, $\bar{\gamma} = 0.3$.

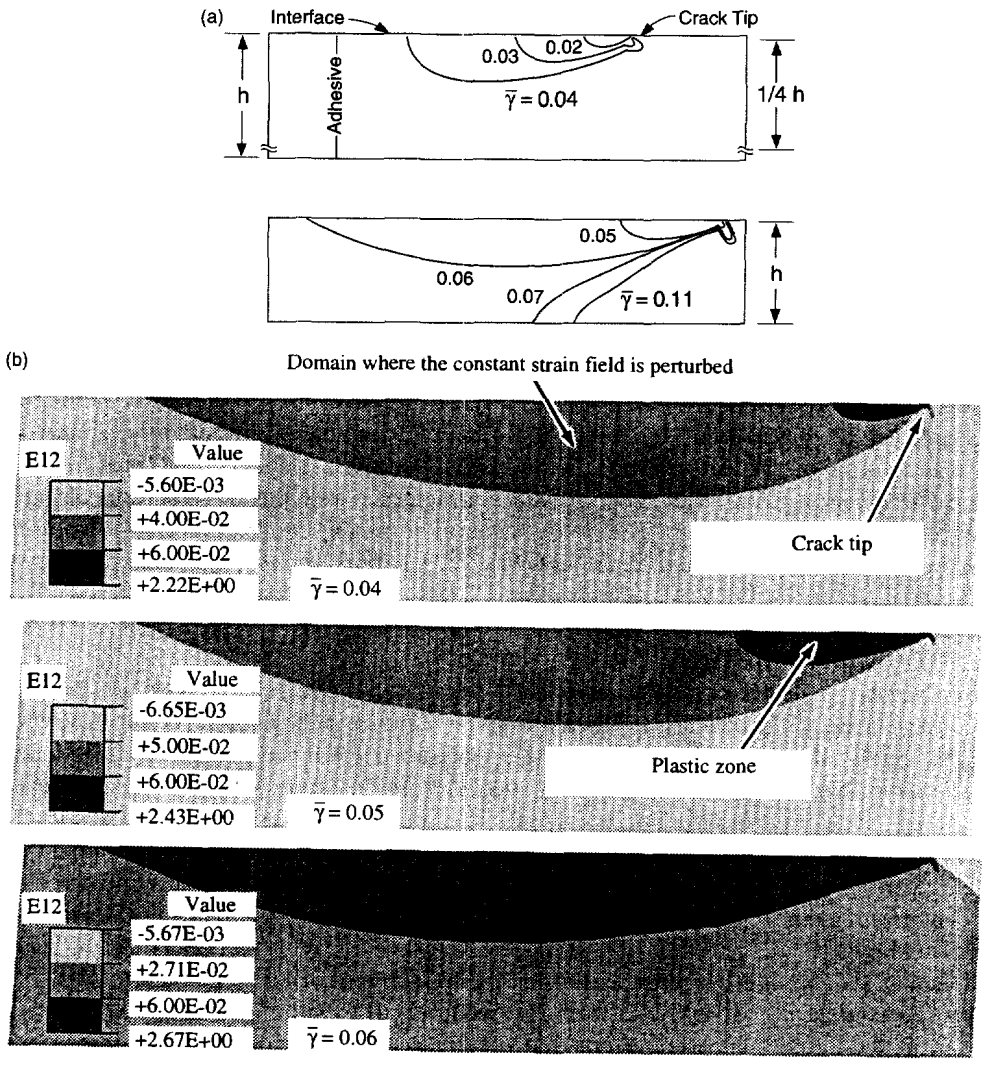

Fig. 4. Elastic–plastic boundaries (a) and domains of unperturbed strain field (b) at different loading levels.

type singularity along the interface, the trend of which extends to several bond thicknesses ahead of the crack tip. It is not clear, however, how close to the crack tip this singular behavior is maintained. The distribution of the adhesive shear strain along the interface, in the vicinity of the crack tip, can thus be expressed by the following form:

$$\gamma = K\bar{x}^{-\delta}, \tag{4}$$

where $\bar{x} = x/h$ and K and δ are nondimensional parameters which depend on $\bar{\gamma}$.

Figure 4(a) shows the boundary lines separating the elastic and the plastic deformations for a number of loading levels ($\bar{\gamma} = 0.02$–0.11). For small loadings ($\bar{\gamma} \ll \gamma_Y = 0.06$), the plastic zone resembles a peanut shape similar to that found for a purely bimaterial interface shear crack [e.g. Zywicz and Parks (1990)], except that the lobe behind the crack tip is much smaller than that ahead of the crack tip. This departure is likely to be due to the differing boundary conditions (i.e. a semi-infinite crack in this study vs a Griffith crack in the study by Zywicz and Parks). As the loading is increased, the plastic zone spreads, first mainly along the interface and later also across the interface. The extent to which the presence of the crack perturbs the otherwise uniform strain field in the bond is also shown in Fig. 4(b) for three loading levels. It is interesting to note that the perturbed domain remains nearly fixed up to the onset of global yielding (i.e. $\gamma\gamma_Y$).

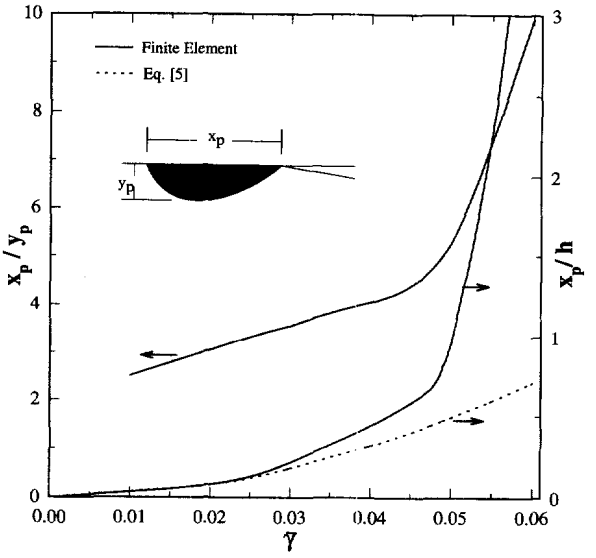

Fig. 5. The variations with $\bar{\gamma}$ of the normalized plastic zone length, x_p, and the slenderness ratio of the plastic zone boundary, x_p/y_p. The data pertain to the CSIC rigid-substrates model.

Figure 5 quantifies the variations of the plastic zone dimensions with load. The slenderness ratio of the plastic boundary (i.e. x_p/y_p, see Fig. 5 for terminology) steadily increases from its small-strain limit of approximately two upon increasing the load. When the applied strain exceeds γ_Y ($=0.06$), global yielding ensues, though the deformations behind and just below the crack tip remains in the elastic range. In their small scale yielding analysis of a constrained metal foil, Varias *et al.* (1991) found that the length of the plastic zone is proportional to the square of the stress intensity factor or load. For the present configuration, this relationship can be expressed as

$$x_p = \alpha(\bar{\gamma}/\gamma_Y)^2. \tag{5}$$

The constant α was determined by matching eqn (5) with the finite element results for $\bar{\gamma} = 0.01$. This gave $\alpha = 0.71$. Figure 5 shows that eqn (5) holds fairly well up to $\bar{\gamma} = 0.03$–0.04.

The analysis shows that a large hydrostatic stress develops at the crack tip, the magnitude of which increases with $\bar{\gamma}$. This stress is tensile for the TSIC model and compressive for the CSIC model. Consequently, the latter case gives rise to a contact between the debonded interfaces behind the crack tip. The development of the bond-normal stress along the contact region with $\bar{\gamma}$ is shown in Fig. 6. Over the range of loading shown, the contact zone remains quite fixed, i.e. approximately four bond thicknesses long, while the contact stress monotonically increases with load. For larger loadings, the normalized length of the contact zone is found to decrease while the contact stress is maintained at the value which is very close to yield stress.

In order to validate the finite element analysis, the limit case of infinitesimally small deformation is simulated by employing a very small load (i.e. $\bar{\gamma} = 0.005$). The corresponding value of δ was determined by drawing a straight line on the log γ vs log x/h plot starting from the end of the plastic zone. The results for the CSIC and the TSIC models are in the range 0.488–0.50 and 0.46–0.47, respectively. The K dominance zone [i.e. the applicability range of eqn (4)] in both cases is found to extend up to approximately 20% of the bond thickness ahead of the crack tip while the contact length, in the CSIC case, is approximately four bond thicknesses long (Fig. 6). In her analysis of a semi-infinite crack separating two isotropic, linearly elastic materials, Comninou (1977) showed that interfacial friction affects the strength of the singularity according to:

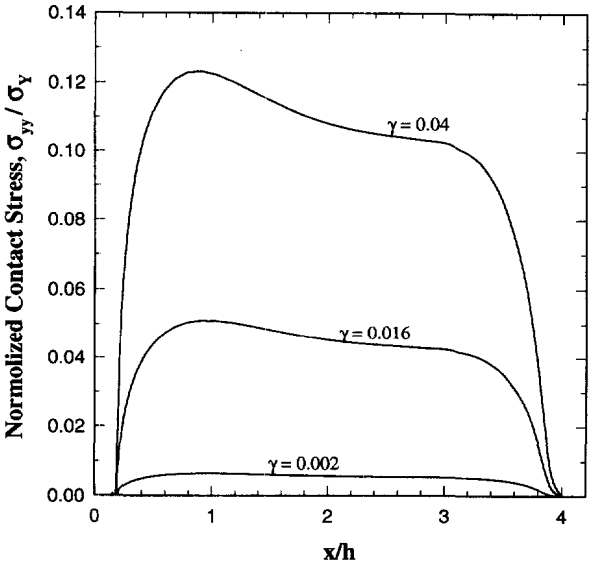

Fig. 6. The distribution of bond-normal contact stress behind the crack tip for three loadings—CSIC rigid-substrates model.

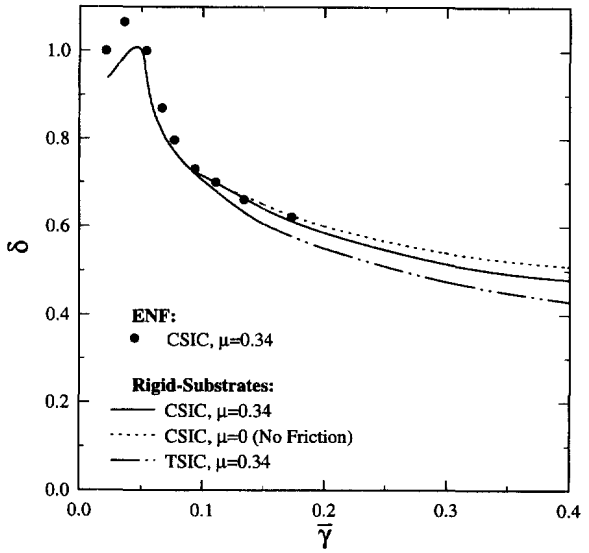

Fig. 7. The variation of the singularity power δ [eqn (4)] with the average shear strain in the interlayer.

$$\cot \pi\delta = n\mu\beta, \tag{6}$$

where μ is the coefficient of friction, n equals $+1$ and -1 for the TSIC and the CSIC model, respectively, and β is one of Dundurs' parameters. For an adhesive having a Poissons' ration equals 0.35 on top of a rigid substrate, $\beta = -0.23$. Using the experimentally determined value of μ (0.34), we find δ equals 0.525 and 0.475 for the CSIC and the TSIC model, respectively. These values, which amount to only a small correction over the classical free boundary case (0.5), are reasonably close to the present results (i.e. 0.488–0.5 and 0.47).

Figures 7 and 8(a) show the variations of δ and K with $\bar{\gamma}$. The results, which include compression and tension side interface cracks as well as one frictionless case ($\mu = 0$), display a number of interesting trends:

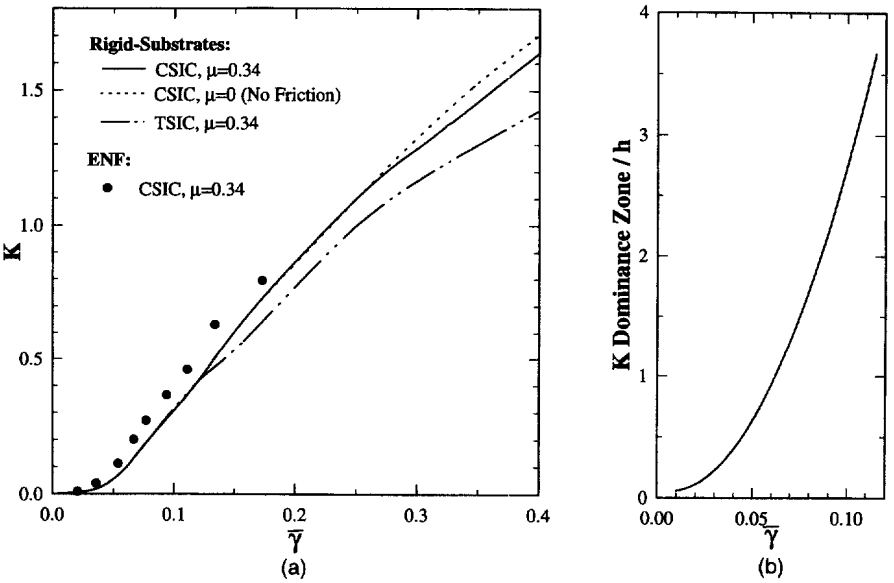

Fig. 8. The variation of K [eqn (4)] with the average shear strain in the interlayer (a) and the variation with load of the K dominance zone [i.e. the range of x/h for which eqn (4) holds] (b).

(1) For small loadings ($\bar{\gamma} < 0.04$–0.05), $\delta \approx 1$. This value coincides with the HRR solution pertaining to a homogeneous, ideally plastic material under small scale yielding conditions [e.g. Hutchinson (1968); Rice and Rosengreen (1968)] and with the case of a Griffith crack separating an ideally plastic material from a rigid substrate [e.g. Sharma and Varias (1991)]. One observes that this loading range closely matches the applicability range of the small scale yielding solution for the plastic zone (Fig. 5). Figure 7 shows that for larger loadings, δ rapidly decrease from 1, becoming as little as 0.5 at $\bar{\gamma} = 0.4$. This reduction in the strength of the singularity is geometry induced (as opposed to a material induced reduction, i.e. strain hardening, in the HRR analysis), apparently being a consequence of the more intimate interaction of the plastic zone with the surface of the lower substrate. It should be noted that although the entire interlayer region ahead of the crack tip may be in a yield state, the specimen can still carry load because the structure outside the bond is displacement controlled.

(2) Figures 7 and 8(a) show that the effect of friction on δ and K becomes significant only for large $\bar{\gamma}$ (i.e. $\bar{\gamma} > 0.2$). The afore-mentioned fracture experiments and Part II show that strains much greater than this do occur during the stable crack propagation.

(3) The distribution of shear strain straight ahead of the crack tip for the TSIC and the CSIC models is essentially indistinguishable up to $\bar{\gamma} \sim 0.1$. For larger loads, the CSIC model leads to a progressively larger strain concentration than the TSIC model.

The K dominance zone in the plastic deformation regime, defined here as the applicability range of eqn (4), is established by determining how far from the crack tip the strain as presented in Fig. 3 conform to a straight line. Figure 8(b) shows that this zone increases with $\bar{\gamma}$, becoming several bond thicknesses long following the onset of general yielding.

3.2. *ENF specimen*

While for the rigid-substrates models the average shear strain is constant throughout the bondline, for the ENF specimen $\bar{\gamma}$ gradually diminishes as one moves away from the crack tip. Consequently, the elastoplastic behavior starting from several bond thickness away from the crack tip is no longer well approximated by the rigid-substrates models. The finite element mesh at the crack tip vicinity is similar to that in Fig. 1(e). The external loading variable here is U, the vertical displacement under the mid-span load, P. The displacement rate, dU/dt, is sufficiently small (2.2 μm s^{-1}) to ensure quasistatic conditions. Comparison with the rigid-substrates models is made on the basis of an equal average shear

strain at the crack tip. The latter quantity, denoted as $\bar{\gamma}_t$, is evaluated from the displacement of appropriate nodes in the finite element grid. Figures 7 and 8(a) (filled circles) show results for $h = 420$ μm. The data for δ and K agree to within a few percent with the rigid-substrates solution. Thus, on a bond thickness normalized length scale basis, at the immediate crack tip vicinity the elastoplastic fields for the ENF specimen appear to be independent of h. The results for the ENF and the rigid-substrates models are found to significantly depart starting from a few bond thicknesses ahead of the crack tip. This departure is of special importance when failure mechanisms initiating ahead of the crack tip are of concern (Part II).

4. CORRELATION WITH THE EXPERIMENTS

It was previously shown that non-local quantities associated with the ENF specimen, such as the length of the plastic zone and the distribution of average shear strain within the zone compare well with the experimental results [e.g. Chiang and Chai (1994)]. The present analysis, which focuses on the local behavior, offers a more scrutinized comparison. Figure 9 shows the deformation pattern at the crack tip region from a fracture test (a) [e.g. Chai and Chiang (1996)] and from the finite element analysis pertaining to the rigid-substrates model (b). Both figures pertain to the same configuration (CSIC) and the same average shear strain at the crack tip, $\bar{\gamma}_t$ ($=0.11$). The similarity in the deformation pattern between the experiment and the analysis is noted. The variation of the local shear strain along the interface ahead of the crack tip for the experimental and the finite element data of Fig. 9 are given in Fig. 10. The correlation between the theory and the experiment seems quite good except for approximately a tenth bond thickness long zone immediately ahead of the tip, where the analytical strain seem to increase beyond bounds while the experimental one changes relatively little. However, as noted earlier, the applicability of eqn (4) in that range has not been determined in this work.

5. SUMMARY AND CONCLUSIONS

Full-field, plane strain elastoplastic solutions for an interface crack in adhesive bonds undergoing extensive shearing are obtained using a large strain finite element program. The adhesive modeled is nearly elastic perfectly plastic, obeying J_2 plasticity. Both rigid and compliant substrates are analyzed. The plastic deformation at the crack tip, although highly

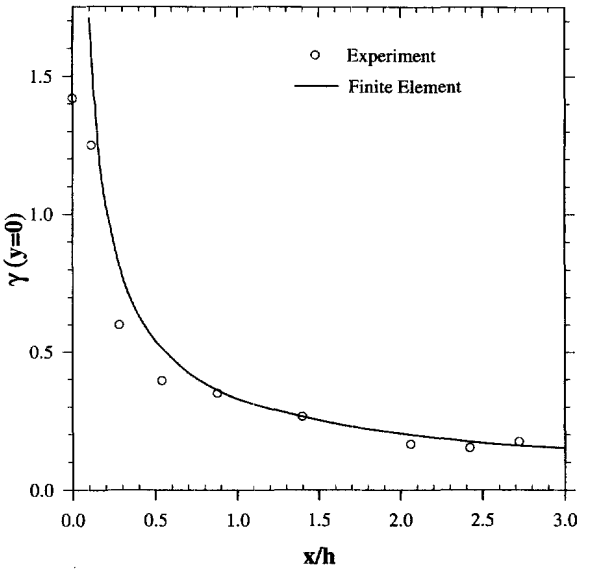

Fig. 10. The distribution of the engineering shear strain along the interface ahead of the crack tip corresponding to the experimental and the finite element data of Fig. 9.

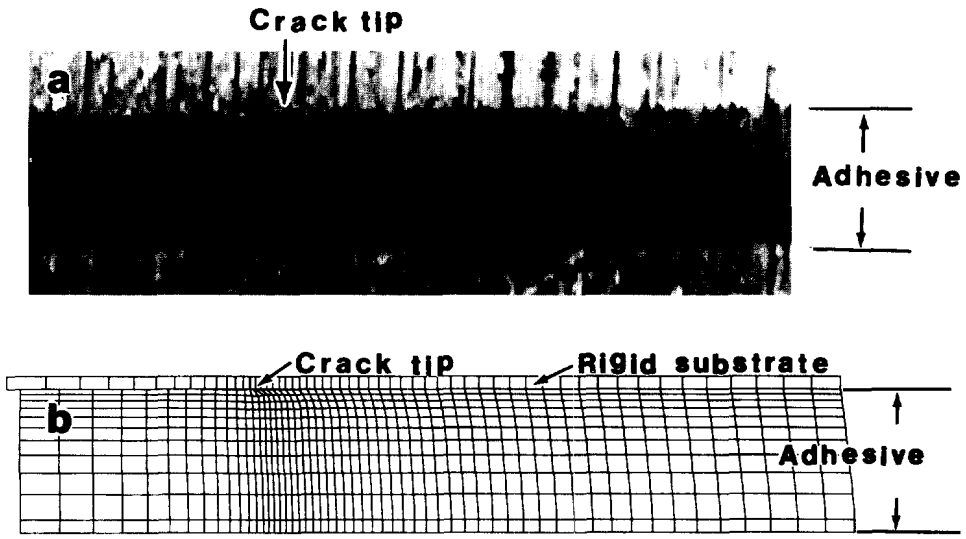

Fig. 9. A video micrograph of the crack tip region from a Butterfly test [Chai and Chiang (1996)], (a), and the deformation grid from the CSIC rigid-substrates finite element model, (b) $h = 262\ \mu m$, $\bar{\gamma}_i = 0.11$.

triaxial, is shear dominated, being confined at the initial stages of loading to a narrow zone along the interface ahead of the crack tip.

The distribution of the engineering shear strain along the interface ahead of the crack tip conforms to a power law singularity of the form $K(x/h)^{-\delta}$ under small scale as well as large scale yielding conditions. This representation, verified to apply as close as a tenth bond thickness to the crack tip, holds equally well for both the CSIC and the TSIC bond configurations, although the amplitude (K) and the strength of the singularity (δ) may differ.

Equation (4) is found to compare well with experimental evidence pertaining to the crack tip region. The results indicate that small strain solutions such as the HRR may be limited to remote strains not exceeding a few percent. For larger remote strains, δ declines monotonically with increasing $\bar{\gamma}$, apparently because of a strong interaction of the crack tip stress filed with the surface of the opposing substrate. This geometry-induced weakening of the strength of the singularity is analogous to that associated with material (strain hardening) weakening which is predicted by the HRR theory.

The rigid-substrates models provide accurate, bond thickness independent elastoplastic solutions to more complex polymer/metal joints such as the ENF and the Butterfly. This agreement, however, is limited to the immediate crack tip vicinity. Where accurate stresses or strains a few bond thicknesses away from the crack tip are needed, the fully-fledged ENF specimen must be considered. The effect of friction and contact between the debonded interfaces seem significant only for relatively large loadings ($\bar{\gamma} > 0.2$). In Part II, it is shown that such load levels do occur during the stable crack propagation phase. Finally, this study may be useful as guidance for developing analytical solutions for the near tip deformation.

REFERENCES

ABAQUS version 5.3 (1994) Hibbit, Karlsson and Sorensen, Providence, RI.

Chai, H. (1992) Micromechanics of shear deformations in cracked bonded joints. *International Journal of Fracture*, **58,** 223–239.

Chai, H. (1993) Deformation and failure of adhesive bonds under shear loading. *Journal of Materials Science*, **28,** 494–506.

Chai, H. and Chiang, M. Y. M. (1996) A crack propagation criterion based on local shear strain in adhesive bonds subjected to shear. *Journal of the Mechanics and Physics of Solids*, **44,** 1669–89.

Chiang, M. Y. M. and Chai, H. (1994) Plastic deformation analysis of cracked adhesive bonds loaded in shear. *International Journal of Solids and Structures*, **31,** 2477–2490.

Comninou, M. (1977) Interface crack with friction in the contact zone. *Journal of Applied Mechanics*, **44,** 780–781.

Goland, M. and Reissner, E. (1944) The stresses in cemented joints. *Journal of applied Mechanics*, **A,** 17–27.

Hart-Smith, L. J. (1981) Stress analysis: a continuum mechanics approach. In *Development in Adhesives*, Vol. 2, ed. A. J. Kinloch, pp. 1–44. Applied Science Publishers, London.

Hutchinson, J. W., (1968) *Journal of Mechanics and Physics of Solids*, **16,** 13–31.

Kuo, A. Y. and Wang, S. S. (1985) A dynamic hybrid finite element analysis for interfacial cracks in composites. In *ASTM STP* 876, 5–34.

Malyshev, B. M. and Salganic, R. L. (1965) The strength of adhesive joints using the theory of cracks. *International Journal of Fracture*, **1,** 114–128.

Pae, K. D. and Bhateja, S. K. (1971) *Journal of the Macromolecular Science*, **C13** (I) 1–75.

Rice, J. R. and Rosengreen, G. F. (1968) Plane strain deformation near a crack tip in a power-low hardening material. *Journal of the Mechanics and Physics of Solids*, **16,** 1–12.

Sharma, S. M. and Aravas, N. (1991) Plane stress elastoplastic solutions of interface cracks with contact zones, *Mechanics of Materials*, **12,** 147–163.

Shih, C. F. and Asaro, R. J. (1988) *Journal of Applied Mechanics*, **55,** 299–316.

Stolarski, H. K. and Chiang, M. Y. M. (1989) On the significance of the logarithmic term in the free edge stress singularity of composite laminates. *International Journal of Solids and Structures*, **25,** 75–93.

Ting, T. C. T. and Symonds, P. S. (1962) Impact of a cantilever beam with strain rate sensitivity. *Proceedings of the Fourth U.S. National Congress of Applied Mechanics*, ASME, Vol. 2, pp. 1153–1165.

Ting, T. C. T. and Chou, S. C. (1981) Edge singularities in anisotropic composites. *International Journal of Solids and Structures*, **17,** 1057–1068.

Ting, T. C. T. (1996) *Anisotropic Elasticity—Theory and Applications*. Oxford University Press, Oxford.

Varias, A. G., Suo, Z. and Shih, C. F. (1991) Ductile failure of constrained metal foil. *Journal of the Mechanics and Physics of Solids*, **9,** 963–986.

Varias, A. G., Suo, Z. and Shih, C. F. (1992) Mode mixity effect on the damage of a constrained ductile layer. *Journal of the Mechanics and Physics of Solids*, **40,** 485–509.

Wang, S. S. and Yuan, F. G. (1983) A singularity hybrid finite element analysis of boundary-layer stress in composite laminates. *International Journal of Solids and Structures*, **19,** 825–837.

Zywicz, E. and Parks D. M. (1990) Elastic–plastic analysis of frictionless contact at interfacial crack tips. *International Journal of Fracture*, **42**, 129–143.

APPENDIX A

Adhesive rate characterization

Uniaxial tension and compression tests were performed on the toughened epoxy adhesive of interest (BP-907, American Cyanamid Co.) to determine the effect of strain rate on the yield stress. Fig. A1 (inset) shows the tensile dog-bone and the cylindrical compression test samples used. The applied strains were limited to a few percent because of the geometrical distortion and inhomogeneity of the deformation (shear banding) that occurred at larger strains. Typical stress–strain curves for the two specimens are given in Fig. A1. The test results, summarized in Table A1, show that the yield stress increases with the strain rate. It is assumed here that the rate dependency is of the form:

$$\dot{\varepsilon}^{pl} = D(\sigma/\sigma_0 - 1)^d \tag{A1}$$

where $\dot{\varepsilon}^{pl}$ is the time derivative of the effective strain and σ and σ^0 are the concurrent and the quasistatic (i.e. $\dot{\varepsilon}^{pl} \to 0$) effective stress, respectively. Taking σ and σ^0 as the compression yield stress at the concurrent $\dot{\varepsilon}$ and at $\dot{\varepsilon} = 3.2 \times 10^{-5}\ s^{-1}$, respectively, it was found, by plotting the test data on a log–log paper, that eqn (A1) holds fairly well for the present adhesive if $D = 10.5$ and $d = 3.7$. The results also show that the yield stress in compression well exceeds that in tension; the ratio σ_c/σ_t being 1.4. This difference reflects the pressure sensitivity of the yield stress, a phenomenon quite common to polymers [e.g. Pae and Bhateja (1971)].

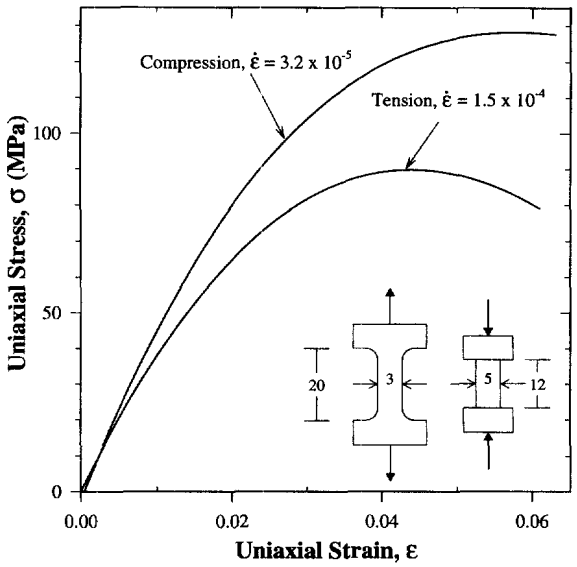

Fig. A1. Typical uniaxial stress–strain curves in tension and compression for the BP-907 adhesive. The inset shows the specimen used. All dimensions are in millimeters.

Table A1. Dependence of yield stress on the strain rate for the BP-907 adhesive

Uniaxial compression		Uniaxial tension	
$\dot{\varepsilon}_c$(1/s)	σ_c(MPa)	$\dot{\varepsilon}_t$(1/s)	σ_t(MPa)
3.2×10^{-5}	128	3.9×10^{-5}	91
1.8×10^{-3}	141	1.5×10^{-4}	99
3.5×10^{-3}	140	2.1×10^{-4}	94
0.021	149	—	—
0.21	175	—	—

Note: The subscripts "c" and "t" denote compression and tension, respectively.

APPENDIX B

Interfacial friction tests

Figure B1 (inset) illustrates the test configuration used to quantify the effect of friction between the debonding interfaces in the adhesive bond tests. Square test pieces having 3×3 mm contact area were cut from fractured ENF specimens. The cuts were made a few millimeters ahead of the tip of the precrack, where the fracture

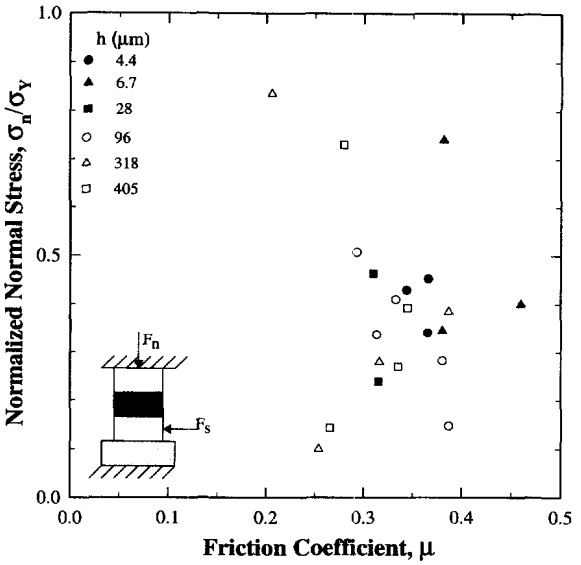

Fig. B1. The dependence of the friction coefficient for the debonded interface on the bond thickness and the applied normal stress. The inset shows the test specimen used. All dimensions are in millimeters.

morphology corresponds to a stable crack propagating. Matched pairs of pieces from above and below the debonded interface were used in each test to insure a consistent morphology. The test samples were first subjected to a given normal stresses, σ_n ($=F_n/A$, where F_n and A are the applied normal load and the contact area, respectively). Then, a monotonically increasing shearing load, F_s, was applied until a sliding motion between the two test pieces occurred. The latter event was easily identified from a real time record of F_s vs F_n. The friction coefficient, μ, was determined from eqn (2), where F_{sc} is the shearing force at the onset of sliding. Results were obtained for various bond thicknesses. In each case, a number of compression preloads were employed. Figure B1 shows μ as a function of σ_n/σ_Y, where σ_Y ($=129$ MPa) is the adhesive static yield stress in compression. Within experimental scatter, the friction coefficient seems little affected by the bond thickness or the applied normal stress. A nominal value of 0.34 for μ was assumed in the analysis.